Computers in Biology and Medicine 40 (2010) 37–53

Contents lists available at ScienceDirect

Computers in Biology and Medicine

journal homepage: www.elsevier.com/locate/cbm

Computerized method for nonrigid MR-to-PET breast-image registration

M.Z. Unlu [a,*], A. Krol [b], A. Magri [c], J.A. Mandel [d], W. Lee [b], K.G. Baum [e], E.D. Lipson [c], I.L. Coman [f], D.H. Feiglin [b]

[a] Department of Electrical and Electronics Engineering, Izmir Institute of Technology, Urla, Izmir 35430, Turkey
[b] Department of Radiology, SUNY Upstate Medical University, Syracuse, NY 13210, USA
[c] Department of Physics, Syracuse University, Syracuse, NY 13244, USA
[d] Department of Civil Engineering, Syracuse University, Syracuse, NY 13244, USA
[e] Chester F. Carlson Center for Imaging Science, Rochester Institute of Technology, Rochester, NY 14623, USA
[f] Department of Psychiatry and Behavioral Sciences, SUNY Upstate Medical University, Syracuse, NY 13210, USA

ARTICLE INFO

Article history:
Received 10 October 2008
Accepted 26 October 2009

Keywords:
MR-to-PET nonrigid breast-image registration
FEM-based soft tissue multimodality nonrigid image registration

ABSTRACT

We have developed and tested a new simple computerized finite element method (FEM) approach to MR-to-PET nonrigid breast-image registration. The method requires five–nine fiducial skin markers (FSMs) visible in MRI and PET that need to be located in the same spots on the breast and two on the flanks during both scans. Patients need to be similarly positioned prone during MRI and PET scans. This is accomplished by means of a low gamma-ray attenuation breast coil replica used as the breast support during the PET scan. We demonstrate that, under such conditions, the observed FSM displacement vectors between MR and PET images, distributed piecewise linearly over the breast volume, produce a deformed FEM mesh that reasonably approximates nonrigid deformation of the breast tissue between the MRI and PET scans. This method, which does not require a biomechanical breast tissue model, is robust and fast. Contrary to other approaches utilizing voxel intensity-based similarity measures or surface matching, our method works for matching MR with pure molecular images (i.e. PET or SPECT only). Our method does not require a good initialization and would not be trapped by local minima during registration process. All processing including FSMs detection and matching, and mesh generation can be fully automated. We tested our method on MR and PET breast images acquired for 15 subjects. The procedure yielded good quality images with an average target registration error below 4 mm (i.e. well below PET spatial resolution of 6–7 mm). Based on the results obtained for 15 subjects studied to date, we conclude that this is a very fast and a well-performing method for MR-to-PET breast-image nonrigid registration. Therefore, it is a promising approach in clinical practice. This method can be easily applied to nonrigid registration of MRI or CT of any type of soft-tissue images to their molecular counterparts such as obtained using PET and SPECT.

1. Introduction

1.1. Breast cancer imaging

Breast cancer is the most common form of cancer among women in the United States [1,2]. X-ray mammography is the primary – highly sensitive but not very specific – way to screen and diagnose breast cancer. When a suspicious abnormality is detected, additional imaging and biopsies are necessary [3]. Breast biopsy is a highly specific and sensitive method, but it is an invasive and sometimes painful procedure, leaving scar tissue that can confound future breast exams. About half the time, it is negative [4–8]. Therefore, it is desirable to have an alternative, noninvasive method to follow up equivocal or difficult-to-interpret X-ray mammograms, or any other inconclusive breast examination. Such methods include F-18-FDG PET [9–13] and MRI [14,15] since both are well-established methods for breast cancer detection in their own rights. MRI provides high sensitivity (95–99%) and variable specificity (50–92%), while F-18-FDG-PET demonstrates variable sensitivity (63–95%) and high specificity (80–95%) [16]. Therefore, it is reasonable to conjecture that the combination of F-18-FDG PET with MRI and perhaps with some other noninvasive breast examination methods (e.g. breast SPECT or magnetic resonance spectroscopy) might provide sufficient diagnostic specificity to allow substitution of breast biopsy with a set of noninvasive imaging procedures. Indeed, Rieber et al. [17] noted that the findings of either or both methods positively affected patients' surgical treatment in 12.5–15% of cases. Walter et al. [18] reported that the combination of F-18-FDG PET and MRI

* Corresponding author. Tel.: +90 505 747 2740; fax: +90 232 750 6599.
E-mail addresses: zubeyirunlu@iyte.edu.tr, zubeyirunlu@gmail.com, mzunlu@ecs.syr.edu (M.Z. Unlu).

0010-4825/$ - see front matter © 2009 Elsevier Ltd. All rights reserved.
doi:10.1016/j.compbiomed.2009.10.010

decreased retrospectively unnecessary biopsies from 55% to 17%. Moy et al. [16,19] reported that fused PET and MR breast images increased the specificity (from 52% to 95%) but decreased the sensitivity (from 92% to 63%) of a combined examination, compared to MRI alone.

There are ongoing efforts to combine PET and MRI scanners into a single unit [20,21]. It is difficult-to-predict when such devices would be available and how much they would cost. Therefore, it seems appropriate now to develop imaging protocols and image-processing methods that would allow registration and fusion of MR and PET breast images acquired on separate scanners, in order to improve the diagnostic efficacy of both methods.

2. MR-to-PET image registration

The registration of MR images to PET images could be based on extrinsic (prospective) and intrinsic (retrospective) techniques [22–28]. The registration process could also be classified as feature-based or intensity-based. The former rely on the geometric information extracted from images, (e.g. segmented volumes or surfaces, or corresponding meshes) while the latter takes advantage of relationship between intensities in the matched images. Somer et al. [29] proposed a hybrid method for MR-to-PET registration of soft-tissue images that took advantage of CT images already registered to PET that were acquired using a PET/CT scanner. They performed MR-to-CT rigid registration followed by nonrigid (intensity-based) registration and utilized the obtained MR-to-CT transformations to register MR-to-PET images and concluded that it improved registration accuracy over direct rigid-only MR-to-PET registration.

There are relatively few publications on monomodal and multimodal breast registration. Zuo et al. [30] performed rigid registration on MR-to-MR breast images acquired in dynamic breast studies employing the approach of Woods et al. [31], relying on minimization of the variance of intensity ratios. Kumar et al. [32] performed nonrigid registration of two breast MR images by minimizing the sum of squared intensity differences between the images. Rueckert [33] reported MR-to-MR registration in dynamic MR breast imaging using affine transformation for the global breast motion, and free-form deformation based on B-splines for the local breast motion. A modification of this approach that assured preservation of the volume was reported by Rohfing et al. [34]. Validation studies of the aforementioned methods were performed by Tanner et al. [35]. Normalized mutual information was used as a similarity measure. The fluid flow [36] and optical flow [37] techniques have also been applied to MR-to-MR breast-image registration. All these approaches rely on well-defined relationships between voxel intensities between the images being registered and all involve optimization. Therefore, they require a good initialization, might be trapped by local minima and tend to be computationally expensive. Due to differences in resolution of PET and MRI, as well as vastly different image formation processes, intensity relationships in PET and MR images are ill defined. Consequently, such techniques, which rely on similarity measures, generally provide unsatisfactory results for nonrigid MR-to-PET registration of soft tissue.

We have reported initial results on MR-to-PET breast-image registration [38–42] using our approach based on the finite element method (FEM) and using up to nine external fiducial skin markers per breast. The mean registration error was estimated, using elastic phantom and patient data, at approximately 5 mm. Noz and colleagues [16,19,43] reported results of MR-to-PET breast-image registration using their landmark-based nonrigid registration method [44]. Between 12 and 40 arbitrarily selected cohomologous points per breast were used including "*absolute landmarks located on recognizable anatomic structures* e.g. *a specific part of the nipple" and "relative landmarks-anatomic structures/points relative to an absolute landmark* e.g. *the apex of the left ventricle and skin boundaries*". The method failed in 20% cases reported in [19], and no quantitative estimation of the registration accuracy was provided.

3. Deformable soft tissue models and their application to image registration

Deformable models have been applied to predict mechanical deformations of tissues or organs based on biomechanical tissue properties and to perform nonrigid image registration. They include brain-shift modeling [45,46]; heart-kinetics modeling [47–50]; breast-compression simulation, such as in X-ray mammography [49,51–54]; and breast-image registration [55–57].

A number of studies devoted to modeling deformation of the breast tissue have been recently published [51,53,55,56,58,59]. They have been applied mostly to elastography for obtaining elastic moduli of tissues under compression for tumor detection, or for comparison of deformed MR volumes. In most of these studies, large deformations were considered, and information on patient-specific breast morphology and on elastic-tissue properties was required. Samani et al. [55] proposed a finite element method (FEM) model, based on biomechanical principles, to predict breast-tissue deformations. They described their FEM simulations of the breast qualitatively only using two different approaches. In the first, they used a linear elastic-tissue model to simulate a 50% deformation of the breast. In the second approach, they simulated 8 mm compression of the breast, using a nonlinear tissue model based on the measurements by Wellman [60] of stress–strain relationships in breast tissue. Azar [61] simulated breast deformation for application in MRI-guided biopsy. The geometry of the model was constructed from MR data, and mechanical properties were elucidated using a nonlinear material model. Another approach to modeling breast-tissue deformation was reported by Ruiter et al. [53,58]. They registered 3D MR breast volumes and 2D projections of X-ray mammograms, using 3D FEM simulation of breast deformation, based on a biomechanical model of mammographic compression. The geometry of the model was inferred from MR data, and the compression simulation was formulated using deformation information derived from X-ray mammograms and physical properties of breast tissue. They reported 5 mm registration accuracy. All these physically based deformable breast models have proved to be very difficult to implement, because of complex and patient-specific breast-tissue morphology and highly nonlinear (hyperplastic) and difficult-to-measure elastic properties of different types of tissues in the breast, as well as explicitly unknown boundary conditions [55]. This has limited their acceptance for clinical work.

4. FEM model for MR-to-PET nonrigid breast-image registration

We have developed and implemented an imaging strategy, a suitable simple FEM model, and image-processing algorithms for nonrigid 3D registration of breast images (Fig. 1). It was tested on human subjects under a protocol strictly following federal guidelines and approved by our Institutional Review Board. This approach requires a small number of external fiducial skin

markers (FSMs), visible in PET and MR images, placed on the surface of the examined breast. It does not require difficult-to-obtain information on the patient-specific elastic properties of the breast tissue. To limit relative stress change in the breast between scans, we used practically identical patient supports and similar positioning in both modalities. For this purpose, during PET scans we used an MRI breast coil replica made of Styrofoam (Fig. 2). We estimate that the breast positioning error was 11.5 ± 3.0 mm, with corresponding relative stress change in the breast of $37 \pm 2\%$ (Section 6.1.5). Under these conditions, the observed displacements, after rigid alignment of moving and target images, are due to stress change and due to underlying biological and physical differences in the imaging process and in the reconstruction algorithms used, including differences in the scanners' spatial distortion and resolution, and the signal-to-noise ratio [62,63]. Our model compensates for such dissimilarities. In addition, it compensates for displacements resulting from physiological and other motion. It can be classified as a point-based registration method combined with a deformable FEM model.

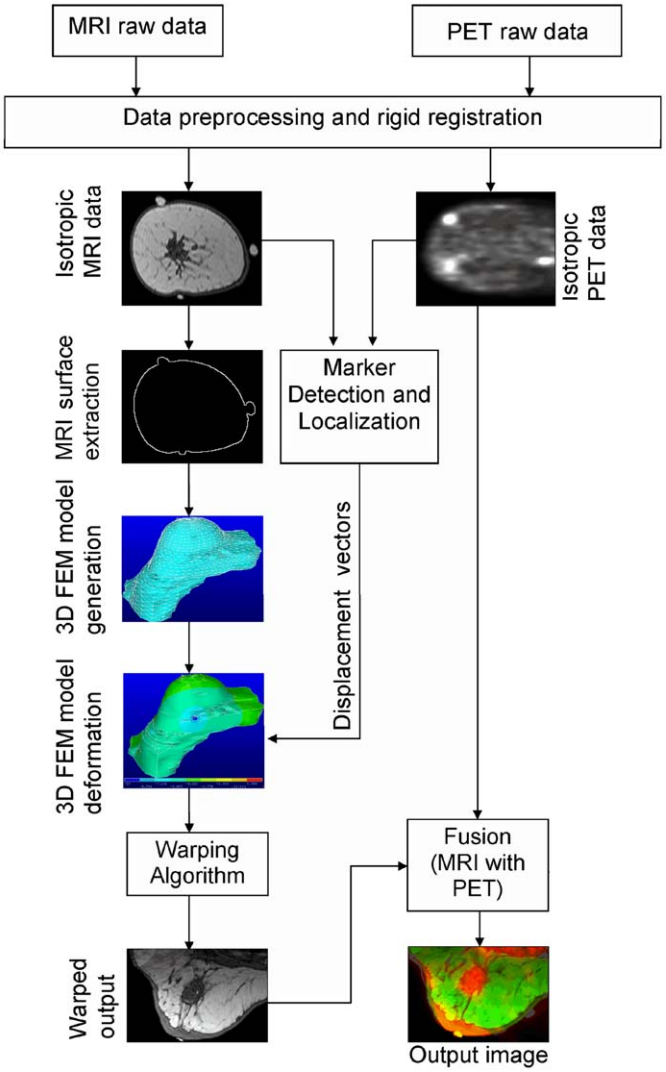

Fig. 1. General block diagram of our deformable finite element method (FEM) model for 3D MR-to-PET nonrigid breast-image registration. Only MR and PET images are required.

Fig. 2. MRI breast coil replica (left) with body support system (right) used during PET scans. It is made of Styrofoam and covered with a polyester cloth.

Table 1
MRI protocol.

Step	Operation
1	Marking in ink locations of FSMs on the breast skin
2	MRI-visible fiducial markers attached on the breasts
3	Patient positioned in prone position in the scanner with breasts dependent but constrained in MRI breast coil
4	IV line placed in antecubital vein (22 or 20 gauge needle) in the side contralateral to the breast with suspicious lesion. Gd-DTPA (Magnevist; Schering AG) is delivered (0.15 mmol/kg) at constant flow 1.5 ml/s directly followed by 20 ml physiologic saline solution after Pre-Gd scan is acquired
5	Field-of-view centered over breasts: $360 \times 360\,mm^2$ except for sagittal images that are $400 \times 400\,mm^2$
6	Breast imaging sequences applied (Table 2)
7	MR image reconstruction. Images are reconstructed by 2D (multislice) or 3D Fourier transforms. K-space data are zero-filled to 256 or 512 complex data points, with a small amount of apodization (ringing filter). Reconstructed image matrix sizes are either 256×256 or 512×512

4.1. MRI and PET/CT data acquisition

4.1.1. Magnetic resonance image acquisition

MRI data acquisition was carried out by a 1.5 T MRI system (Intera, Philips Healthcare) using a standard Philips clinical breast coil without quadrature detection or parallel receiver technology. To acquire the MR data, we followed the acquisition protocol described in Table 1 and used sequences listed in Table 2.

4.1.2. Positron emission tomography image acquisition

PET/CT data acquisition was performed by means of a PET/CT scanner (Discovery ST, GE Healthcare) following the protocols listed in Table 3. One should note that CT data are not required for application of our method in which primary objective is registration of PET and MR images. However, if coregistered PET and CT images are available (from a PET/CT scanner), than the CT data can be used to improve registration accuracy.

4.2. Image preprocessing and rigid registration

Before carrying out the steps of our nonrigid registration algorithm, MRI and PET data sets needed to be preprocessed and rigidly registered. The rigid registration was facilitated by two sets of fiducial skin markers visible in PET and MRI: one located

Table 2
MRI sequences used.

Technique	Resolution	TR/TE/(ET)	Comment
Scout in three planes			Locate anatomy relative to isocenter
HiRes 3D FFE	$320 \times 256 \times 120$ (1.1 mm)	14/3	Isotropic 3D for image fusion calculation
T1 axial TSE	256×256 (4 mm)	750/7/4	Fat suppressed anatomy
T2 axial TSE	256×196 (5 mm)	5600/84/14	Accentuates fluids
Axial 3D SPIR	$320 \times 270 \times 30$ (3 mm)	35/5.2	IR prep.; high resolution anatomy
Left Sag 3D SPIR	$320 \times 270 \times 30$ (3 mm)	35/5.2	IR prep.; high resolution anatomy
Right Sag 3D SPIR	$320 \times 270 \times 30$ (3 mm)	35/5.2	IR prep.; high resolution anatomy
Dynamic GRE	$320 \times 270 \times 70$ (3 mm)	5.4/2.1	Pre-Gd baseline reference
Dynamic GRE	$380 \times 304 \times 70$ (2.53 mm)	5.4/2.1	During Gd–DTPA injection and five more measurements at 90 s intervals

FSMs=Fiducial skin markers, FFE=Fast field echo (a gradient echo technique), [GRE], non-steady state), TSE=Turbo spin echo (a multislice spin echo technique with multiple phase encodings per TR), SPIR=Spectral presaturation with inversion recovery (fat signal suppression). GRE=Gradient recall echo (radio frequency pulse sequence)

Table 3
F-18-FDG-PET/CT protocol.

Step	Operation
1	PET-visible fiducial skin markers taped to the breasts at previously marked (before MRI scan) locations
2	Patient positioned in prone position in the scanner with breasts dependent but constrained in MRI breast coil mold (Fig. 2)
3	Field-of-view centered over breasts
4	10 mCi F-18 FDG injected in the medial antecubital vein (22 or 20 gauge needle) in the side contralateral to the breast with the suspicious lesion
5	CT scout scan: 3 bed positions, 10 s, 120 kVp, 10 mA, followed by landmark setting
6	CT attenuation correction: 1 bed position, 20 s, 140 kVp, 120 mA, and helical scan
7	PET dynamic acquisition: 2D with septa, 10 scans at 5 min each, for total of 50 min; or 50 scans at 1 min each, for total of 50 min
8	Reconstruction: 4.25 mm slice interval, 512×512 matrix, 47 slices per bed position plus 2 slice overlap. Emission was reconstructed with 4.25 mm voxel size, 128×128 matrix, 47 slices per bed position, diameter 60 cm, OSEM algorithm, 30 subsets, 2 iterations, post filter 6.0 mm, loop filter 4.7 mm, with z-axis filter, measured via CT attenuation correction; randoms corrected by singles, correction for dead time, correction for decay, correction for geometry, scatter compensation by fitting, well counter corrected for sensitivity and activity

OSEM=Ordered subsets expectation maximization

Table 4
Methodology of image preprocessing and rigid registration.

Step	Operation
1	Open PET, CT and MR images in axial views
2	Normalize PET data to bring all the slices to the same level of intensity
3	Bring all the images into the same orientation according to MRI data. Obtain stack of images in prone position with slices arranged from posterior to anterior
4	Convert PET, CT, and MRI data to the isotropic matrices with voxel size equal to the voxel size of MRI in x and y direction in axial view
5	Crop the images in 3D according to MRI data. PET and CT image space needs to be of the same size as MR image space
6	Localize matching pairs of fiducial skin markers in PET and MR images and calculate their centroids
7	(i) Create a 3D cropping window in the PET image space with the same size as MR image. (ii) Shift the 3D cropping window appropriately until the distances between the markers and its vertices are the same as the distance between the marker centroids and the vertices of the MR image.

on the left and one on the right flank of the subject. The operations applied in this phase of data processing are listed in Table 4. They were performed automatically using our custom-written plug-in in ImageJ[1] software.

4.3. Fiducial skin markers and their localization

In our research clinical protocol, fiducial skin markers (FSMs) were placed on the study subjects' breast skin in a predefined pattern (Fig. 3) and at two additional locations on the left and right flank. Small crosses were inked on the appropriate locations on subjects' skin with henna to identify marker locations, and the subjects were instructed not to erase them between MRI and PET scans. Separate FSMs were used for MR and for F-18-FDG PET imaging because it was difficult to make one universal FSM visible in both MRI and PET. For MRI scanning, we used custom-made, spherically shaped, gel-based FSMs with diameter $\sim$5 mm. The gel composition was selected by trial and error to minimize the permeability artifacts in the MRI sequences used. Indeed, we have not observed any significant artifacts, e.g. due to chemical shift. For PET imaging, we used custom-made[2], sealed, $\sim$0.5 μCi Ge-68 sources, each contained in a spherical container not exceeding 1 mm in diameter, placed in the center of a flexible transparent plastic disk (1 mm thick and 20 mm in diameter) with a cross-hair printed on it. This amount of activity was selected based on tests with a set of markers each containing activity in the range 0.1–10 μCi. Too much activity in FSM resulted in "hot" spots in the reconstructed images interfering with breast tissue images. Too little activity in a FSM prevented proper visualization of the marker.

The markers taped on the breast surface at the inked locations were used to sample the displacement field between the moving (MR) and the target (PET) images (Fig. 3). The number and location of the markers must be sufficient to properly sample the breast domain. In order to determine the minimum number and acceptable locations of markers necessary to assure good quality registration, we performed target registration error (TRE) vs. number of FSMs analysis (Section 6.1.1). We have established that, depending on the breast tissue volume, 5–9 markers per breast are sufficient to sample the tissue deformation at an acceptable level of error.

The first step of data processing involved display of the PET and MR images in the common coordinate system and identification of the corresponding fiducial skin markers in the target (PET) and in the moving (MR) images. The Euclidian distances between corresponding markers (one visible in MRI and one visible in PET) were calculated for each marker pair and they defined a set of the displacement vectors that were used in our nonrigid FEM-based

[1] http://rsb.info.nih.gov/ij/.
[2] PET fiducial skin markers were provided CTI molecular imaging.

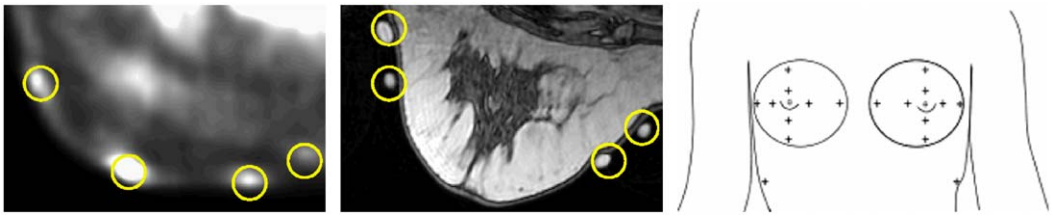

Fig. 3. Images of fiducial skin markers (encircled in yellow) acquired during PET (left panel) and MRI (center panel) for the same subject shown in axial views. Right panel: predefined pattern of fiducial skin markers (crosses) placement on the study subjects' breast skin and flanks shown in coronal view. For interpretation of the references to colour in this figure legend, the reader is referred to the web version of this article.

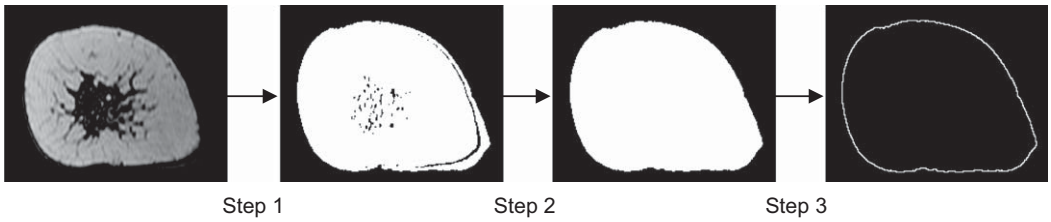

Fig. 4. Example of estimation of patient-specific surface geometry of the breast from coronal sections of the moving (MR) image. Step 1: thresholding; step 2: erosion and dilation operations; step 3: outlining the breast contour.

registration of breast MR to breast PET images. A user who had prior knowledge on the markers' anatomical locations performed manually the procedure of corresponding markers identification.

The second step of data processing dealt with estimation of Cartesian coordinates of PET and MR image centroid for each marker in the common coordinate system. This procedure was performed using the iterative knowledge-based method described by Wang et al. [64]. In this, approach the user first identifies a voxel belonging to a marker, and then the algorithm finds the lowest threshold defining a set of voxels connected in 3D to the selected voxel that could form an object with proper geometrical extent to be a marker. The effective size of a marker's image is defined by its physical size and the spatial resolution of the imaging system. The algorithm estimates the coordinates of the centroid of the image of a marker by calculating location of its geometrical center.

We established that the total time required for manual identification of corresponding skin markers and for calculations[3] of the centroids' locations was about 25–30 s for nine pairs of markers per breast. Recently, we have implemented automated localization of fiducial skin markers using correlation pattern recognition [65]. It further reduced the processing time.

4.4. Estimation of patient-specific surface geometry of the breast

After performing FSMs localization and estimation of the displacement vectors, the patient-specific surface geometry of the breast was obtained from coronal or sagittal MR images for a single breast or both breasts registration, respectively. For 3D fast field echo (FFE) T1-weighted MR sequences without fat suppression, this has been accomplished by global thresholding with a user-selected threshold value. Fig. 4 shows an example of this process. Because we automated this part of image processing, the time required to obtain the patient-specific surface geometry of one breast was about 10 s. For other MRI sequences where the boundaries of the breast tissue are not as clearly defined, more elaborate approaches (e.g. level sets [66]) are needed for segmentation of the breast tissue. Consequently, for each subject a set of coronal and sagittal breast contours was obtained and used to create an input file for the commercial FEM software that we employed.[4]

4.5. Finite element mesh generation in 3D

After obtaining patient-specific surface geometry of the breast, the breast surface and volume was meshed first. Our custom-written plug-in in ImageJ took the set of coronal or sagittal breast contours, prepared in the previous step as an input, and generated the 3D finite element model (FEM) file of the breast to be used as an input by an FEM software, ANSYS. The file contained the geometry of the breast built using key points, splines, and volumes, as well as the definition of the surface and the volume elements, and the displacement vectors. To initialize the algorithm, the plug-in required the user to enter the number of key points for each slice, as well as the slice increment in order to approximate the breast surface using B-splines. After several tests, we decided to choose the number of key points equal to 24 (which corresponds to sampling a surface contour at every 15°), and the slice increment equal to five, while processing a single breast geometry using coronal cross-sections, and equal to eight while processing simultaneously both the left and right breast of the same subject using sagittal cross-sections. Consequently, a patient-specific FEM mesh was created for each study participant (Fig. 5). Two mesh element types have been used in the study: a 3-node triangular shell element for the breast surface, and a 10-node tetrahedral volume element for the interior of the breast (Fig. 6).

4.6. Breast tissue geometric deformation estimation using FEM with fiducial skin markers—only PET and MR images are required

In order to estimate geometric deformation of breast-tissue using the low number of observed MRI–PET displacement vectors, we exploited an analogy between the breast-volume geometric

[3] Performed by custom plug-in written in ImageJ, http://rsbweb.nih.gov/ij/.

[4] ANSYS ver. 5.7.1, ANSYS, Inc. Canonsburg, Pennsylvania.

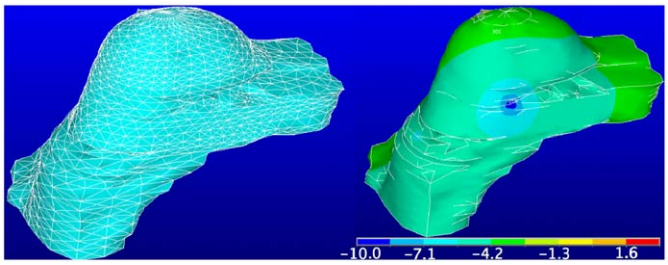

Fig. 5. Left panel: example of meshed breast surface. Right panel: distribution of displacement vectors over entire breast surface. The calibration bar shows the displacement range maximum–minimum vector values. Both images were obtained using the ANSYS FEM software.

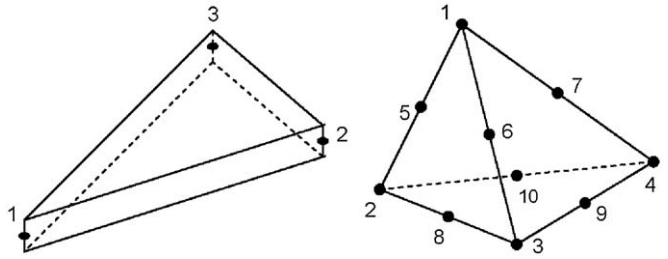

Fig. 6. Left panel: three-node thermal shell mesh element (ANSYS element: SHELL57). Right panel: 10-node tetrahedral thermal-solid mesh element (ANSYS element: SOLID87).

deformation and the temperature distribution in steady-state heat transfer (SSHT) in solids. In this approach, the material properties of the FEM model are the coefficients of "thermal conductivities." Because we are only interested in the "temperature" differences, equivalent in our model to the Cartesian components of the nodal displacement vectors, the *solution is independent of the magnitudes of the material properties*. The breast tissue surface and a small set of the measured displacement vectors ("loads") at FSMs provide the boundary conditions for FEM. In view of the fact that in reality each node of the breast surface is displaced to some degree (not just the nodes next to FSMs) with smooth and slow variation across the surface, one should avoid creating artificial singularities at the locations of the known FSMs. Such singularities would result in nonphysical solutions with incorrectly large displacements (i.e. large local deformations) concentrated near the FSMs. Therefore, one needs to interpolate and extrapolate the displacements from a small set of the measured displacement vectors at the FSM points to a very large number of displacement vectors—one for every surface node. To accomplish this task, a layer of triangular elements (Figs. 5 and 6) is placed at the surface of the breast-tissue mesh. The coefficients of conduction assigned to these elements are arbitrarily set to be 1000-fold greater than those assigned to the solid elements in the interior of the breast. As a result, the surface layer reaches steady state 1000 times faster than the breast interior. We investigated what is the correlation between the surface-to-bulk (S_c/B_c) ratio of thermal conductivities and the solutions obtained, and we have determined that solutions are independent of this ratio for $S_c/B_c > 100$. Using the ANSYS FEM software, the SSHT FEM model was solved three times, once for each of the three orthogonal (x, y, z) directions. The z direction, parallel to the gravity vector during the scans, was roughly perpendicular to the chest wall. The x and y directions were, craniocaudal (from the sternum to the head) and mediolateral (from the sternum to the right shoulder), respectively. As a result of this processing, a dense displacement field (i.e. a displacement vector for every node) was obtained by distributing, piecewise linearly, the Cartesian components of the FSM displacement vectors first over the breast surface, and then throughout its volume. Since a steady state temperature distribution problem is linear, finite element run times were very small. The execution time was about 60 s per Cartesian component for the entire mesh.[5] Such short processing time is vital if the procedure is to be used in a clinical setting.

4.7. Image-warping algorithm—interpolation of the FEM solution

The SSHT FEM computation yields a displacement vector at each node of the finite-element mesh. In order to create a 3D image of the deformed breast, the image-intensity values need to be obtained for every voxel of the breast volume. An image-warping algorithm performs this task. Displacement vectors for each voxel are estimated using a weighted sum of the element's nodal displacements, with the weights equal to the element's node shape function [61,67]

$$u = \sum_{i=1}^{N_{nodes}} N_i^{el} u_i^{el} \tag{1}$$

where N_{nodes} is the number of nodes in the element, N_i^{el} is the element's node shape function, and u_i^{el} is the nodal displacement vector. Finally, the image-intensity values for each voxel are interpolated via a truncated sinc interpolation kernel [68].

4.8. Optional step: breast tissue geometric deformation estimation using a surface-matching algorithm and spatially coregistered CT images

Here, we should clearly point out that our SSHT FEM algorithm is mainly designed for the MR-to-PET breast-image registration. It does not require CT data and it performs well. However, it can also take advantage of additional CT data if available. If coregistered CT data are available (e.g. provided by a PET/CT scanner), as a second optional step, a surface-matching algorithm can be applied to correct for small misregistration (below 4 mm) that can occur in some locations away from FSMs (Fig. 7). In this optional step, the FSM displacements cannot be used, because they had been already aligned. Instead, one can use the displacements observed at selected corresponding surface points, where misregistration between MR- and CT-rendered breast surfaces is detected (Fig. 8).

The displacement vectors estimated for the selected corresponding surface points were used to determine the nonrigid transformation needed to further improve registration of the PET and MRI volumes. For this purpose, the MRI-derived surface regions that exhibited mismatch with the CT-derived surface were determined using a tolerance value set to be equal to the MRI voxel size (0.7 mm). Because the target (PET) and the moving (MR) volumes have already been aligned in 3D using measured FSMs displacements; in this step, a radial method of establishing point correspondence between CT and MRI was used. For this purpose, the selected surface regions that needed to be better matched were first determined and represented by curves in the moving and target image slices. In the second step, the rays originating from the "center of mass" of each MR image slice with a preset angular sampling were used to determine the corresponding points[6] on moving- and target-volume surfaces. The Euclidian distances between the corresponding points on surfaces

[5] Using a 3 GHz, dual Xeon processor PC.

[6] The corresponding points are defined here as the closest points.

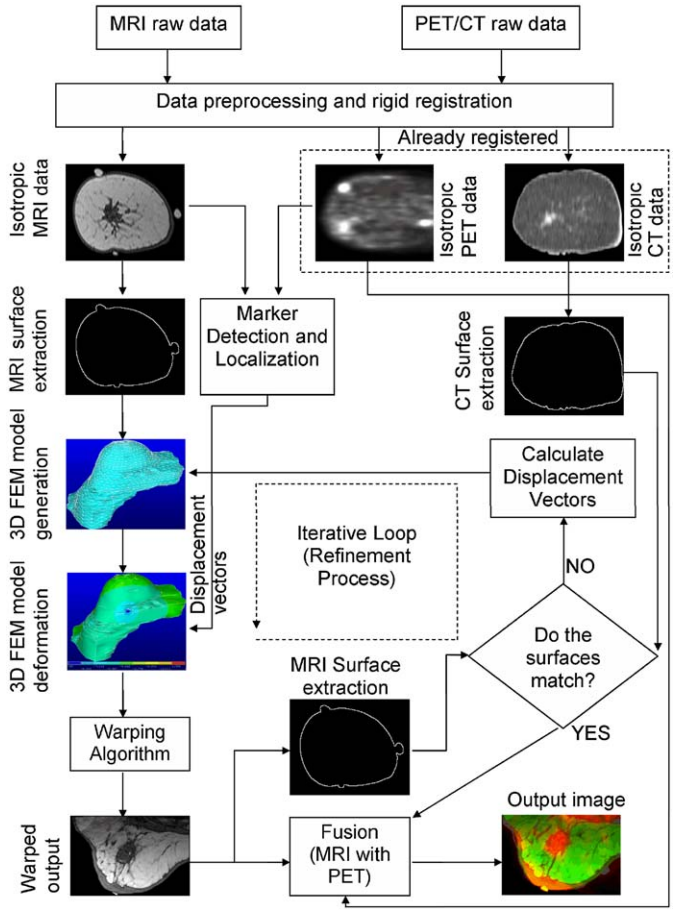

Fig. 7. General block diagram of our iterative deformable finite element method (FEM) model for 3D MR-to-PET nonrigid breast-image registration including the optional MR-to-CT surface matching, if spatially coregistered CT images are available in addition to PET and MR images.

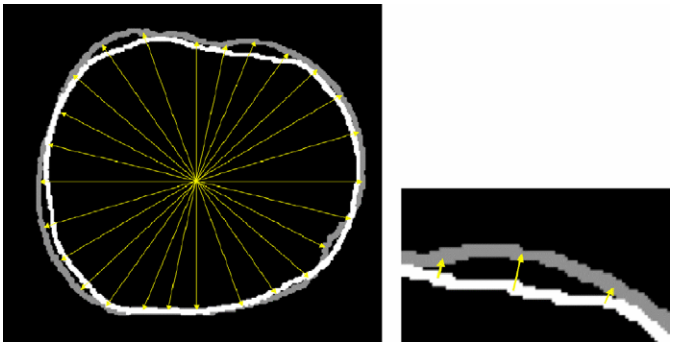

Fig. 8. Left panel: definition of corresponding points on surfaces of moving (MR) and target (PET) images (see text). Gray: breast surface obtained from CT image (acquired by PET/CT scanner). White: breast surface obtained from MRI. Right panel: partial zoomed view of displacement vectors obtained for previously defined (left panel) corresponding points on the surfaces.

visible in MR and CT images provided a new set of displacement vectors. Consequently, they were used as "loads" in our SSHT FEM model (Sections 4.5 and 4.6) and the moving (MR) image was geometrically deformed for a second time.

5. Experimental studies

5.1. Study participants

We have acquired PET/CT and MRI data with fiducial skin markers on 15 human subjects under an approved Institutional Review Board protocol. We have tested our method on 15 consecutive subjects that were enrolled in our protocol (the mean age was 54.3 ± 11). The total number of participants was limited by the amount of funding available. We have not selected "the best" data matching our study design. Rather, we processed all participants' data in the same way without any prejudice. The majority of the subjects were referred for evaluation for participation in the study protocol from the Comprehensive Breast Care Center at SUNY Upstate Medical University Hospital. Subjects seen at the Breast Care Center who were found to have either a suspicious palpable breast mass, or a suspicious mammogram, or a suspicious ultrasound finding were evaluated for this study. Specifically, we were looking to enroll subjects with a prior history of breast cancer, or a strong family history of breast cancer, or a difficult-to-interpret, dense or inconclusive mammograms warranting a biopsy. No restriction of participation by race or ethnic origin was anticipated or desired in this study. The restrictions for inclusion, exclusion, and elimination of data to be used in the study are listed below.

Inclusion criteria:

(i) Difficult-to-interpret, dense or inconclusive mammography, or a suspicious mammogram, or ultrasound, or suspicious palpable breast mass, or a prior history of breast cancer, or a strong family history of breast cancer.
(ii) Warranting a breast biopsy.
(iii) Age: 21 years and above
(iv) Gender: females.
(v) Ethnic/racial: any.

Exclusion criteria:

(i) Weight higher than 300 lbs (scanner size restriction).
(ii) Cardiac pacemakers or other non-compatible with MRI metal artifacts.
(iii) Claustrophobic subjects.
(iv) Pregnancy, breast-feeding, or if there is a chance of becoming or being pregnant.
(v) Subjects unable to tolerate positioning for the procedures due to physical ailment.

Elimination criteria:

(i) Voluntary departure by the subject.
(ii) Women of childbearing potential who are not practicing a medically accepted method of birth control are encouraged not to participate (since there is a risk of becoming pregnant).
(iii) At the request of the medical director of this project, if the subject does not comply with the requirements of the imaging studies, as outlined in the consent document.

5.2. Imaging studies

The MR studies were performed with a 1.5 T MR scanner (Intera, Philips Healthcare) running version 8.1.3 software with "master gradient" hardware and a standard clinical breast coil without quadrature detection. For PET/CT studies, we used a PET/

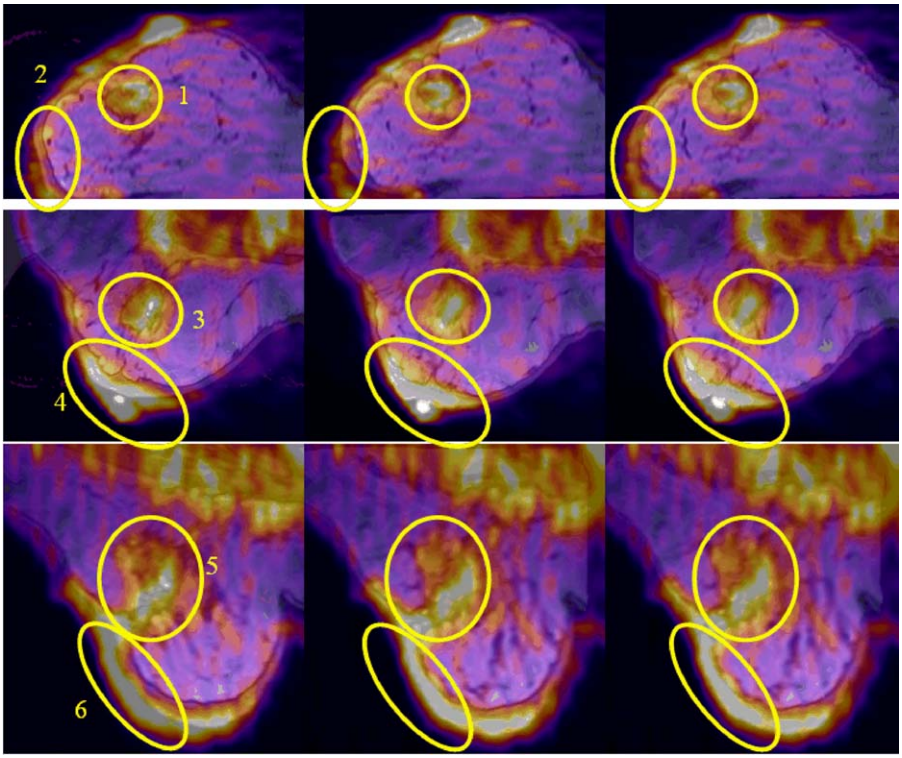

Fig. 9. Subject #1: comparison of fused functional (PET) and anatomical (MR) breast images. Pixel size: 0.7 mm. Regions of interest are marked by yellow ellipses. First column: after rigid registration only. Second column: after our finite-element model deformation method using fiducial skin markers. Third column: after optional MR-to-CT surface matching. Subject #1 is 58 years old with focal atypical ductal hyperplasia, sclerosing adenosis, fibrocystic changes, microcalcifications, fibrocystic changes, and microcalcifications, with history of recurrent ductal carcinoma in situ. For interpretation of the references to colour in this figure legend, the reader is referred to the web version of this article.

CT (Discovery ST, GE Healthcare) scanner with a BGO detector (Section 4.1).

5.3. Image processing

We have tested the performance of our FEM MR-to-PET breast-image registration method using MR[7]-derived breast volumes (moving images) and F-18-FDG-PET volumes (target images). MRI sequences without fat suppression (e.g. 3D FFE) were the easiest to use, because the skin could be easily segmented via global thresholding, thus providing an accurate data on breast surface.

After identification of the corresponding fiducial skin markers (five or nine pairs per breast) in the target (PET) and in the moving (MR) images, their geometric centroids were estimated using Wang's method [64] and a sparse, discrete displacement field (five or nine vectors per breast) was obtained (Section 4.3). These data allowed our FEM model to estimate a dense displacement field (i.e. to calculate a displacement vector for each mesh node), which in turn was used to geometrically deform (warp) the moving MR image in 3D to match the target PET image.

In order to jointly display the coregistered breast volumes, the registered PET and MR images were fused using the KGB Fusion Viewer[8] program. The registered images have been fused using a frame-by-frame approach; a "fire" look-up color table (LUT) has been used to display low-resolution functional F-18-FDG-PET data, and gray scale has been used to display high-resolution anatomical MRI data. They were averaged with equal weight.

Examples of fused MR and PET breast images obtained for three randomly selected study subjects can be found in Figs. 9–11. They provide the comparison of registered and fused molecular (PET) and anatomical high-resolution (MR) breast images after rigid registration only (first column), using only PET and MRI data (second column), and using PET and CT data (after optional MR-to-CT surface matching, third column). Visual inspection of the regions of interest (ROIs) labeled 1, 3, 5, and 7–12 leads to the conclusion that the standardized uptake values (SUVs) of F-18-FDG in the glandular tissue of the breast imaged in PET do not correlate well with the observed morphology of the breast glandular tissue imaged by MR, after rigid registration only. In contrast, the images shown in the second and third columns indicate that application of our method yields improved registration of the enhanced metabolic activity regions revealed by PET with the well-defined glandular tissue demonstrated by high-resolution MRI, in comparison to rigid registration only. Inspection of ROIs labeled as 2, 4, 6, and 8 reveals the improved registration of the surface regions away from FSMs where misregistration was present after using only PET and MR images. The resulting images demonstrate that the optional MR-to-CT surface-matching step – a refinement using a CT-derived-to-MRI-derived volume-matching algorithm – improves not only the surface but also the volume registration.

The total processing time including second iteration was about 15 min per subject.[9]

[7] Including high-resolution 3D FFE, T1 Axial TSE, T2 Axial TSE, and dynamic GRE sequences (Table 2).

[8] http://www.kgbtechnologies.com/fusionviewer/

[9] Based on using a Dell Precision 670 workstation with a dual-core 3.6 GHz Xeon processor.

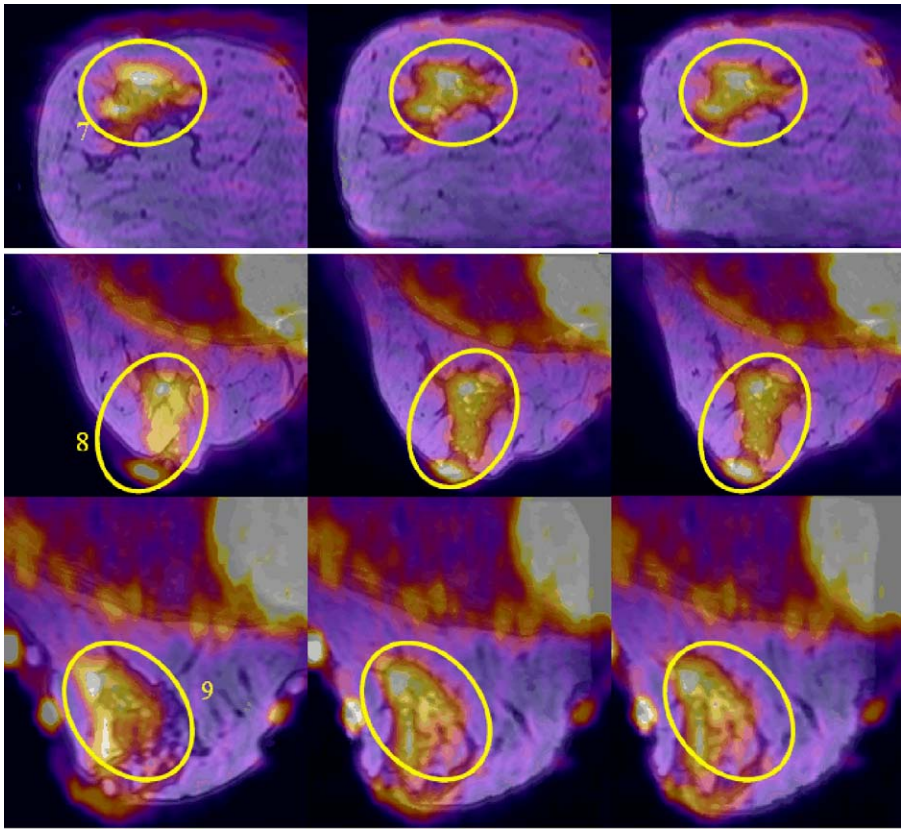

Fig. 10. Subject #2: comparison of fused functional (PET) and anatomical (MR) breast images. Pixel size: 0.7 mm. Regions of interest are marked by yellow ellipses. First column: after rigid registration only. Second column: after our finite-element model deformation method using fiducial skin markers. Third column: after optional MR-to-CT surface matching. Subject #2 is 59 years old with scattered fibroglandular tissue but no focal masses, and a very strong family history of breast cancer. For interpretation of the references to colour in this figure legend, the reader is referred to the web version of this article.

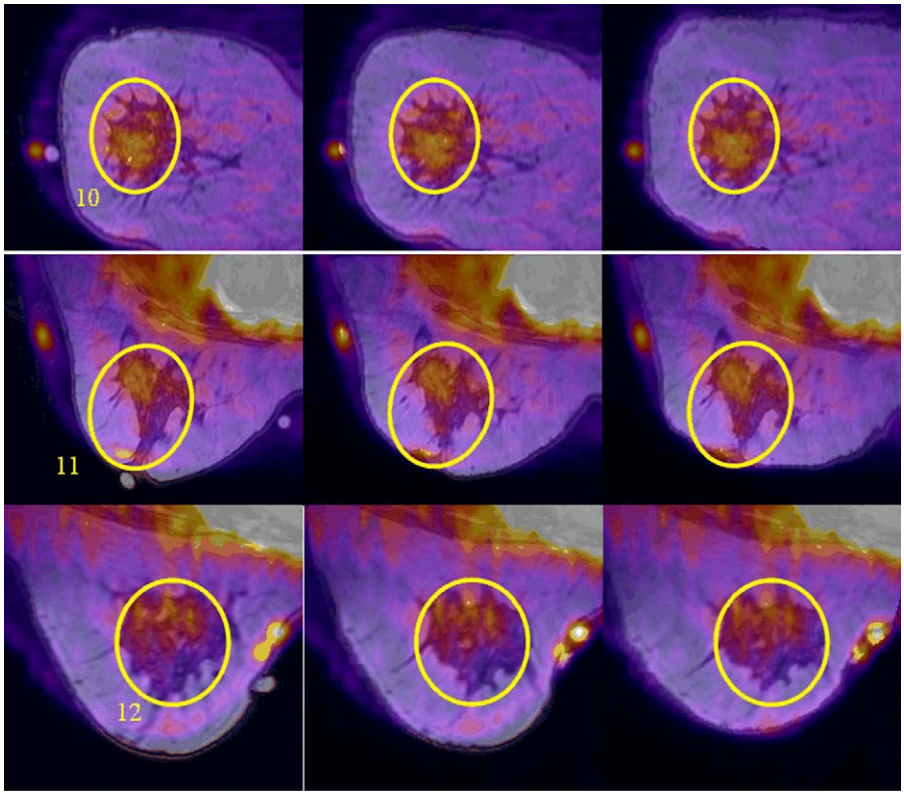

Fig. 11. Subject #3: comparison of fused functional (PET) and anatomical (MR) breast images. Pixel size: 0.7 mm. Regions of interest are marked by yellow ellipses. First column: after rigid registration only. Second column: after our finite-element model deformation method using fiducial skin markers. Third column: after optional MR-to-CT surface matching. Subject #3 is 62 years old with no mammographic evidence of malignancy, with bilateral benign stable microcalcifications, and with lobular carcinoma in situ in the past. For interpretation of the references to colour in this figure legend, the reader is referred to the web version of this article.

6. Performance analysis of our FEM registration algorithm

The qualitative and quantitative methods used in evaluation of the performance of our registration algorithm are listed in Table 5.

6.1. Error analysis

We performed five different error analyses: (i) target registration error vs. number of fiducial skin markers study that evaluated performance of our registration method vs. the number of FSMs; (ii) target registration error vs. fiducial skin marker localization error that estimated error that was introduced when the fiducial skin markers were localized with various amount of uncertainty; (iii) errors analysis in fiducial markers co-location between PET and MRI; (iv) convergence analysis that investigated dependence of the target registration error on the number of FEM mesh nodes used; (v) assessment of the internal stress change in the breast tissue as a function of the breast positioning.

Table 5
The qualitative and quantitative methods used in evaluation of the performance of our registration algorithm.

Analysis	Intensity-based similarity measures	Qualitative surface similarity estimates
1. Target registration error vs. number of fiducial skin markers (TRE vs.♯ of FSM) 2. Target registration error vs. fiducial localization error (TRE vs. FLE) 3. Marker co-location error analysis 4. FEM solution convergence analysis 5. Estimation of breast positioning error and related stress change in the breast	1. Mutual information (MI) 2. Normalized mutual information (NMI)	1. Isoprojected surface similarity plot (ISS) 2. Normalized polar surface similarity plot (NPSS) 3. *z*-Axis surface similarity plot

6.1.1. Target registration error vs. the number of fiducial skin markers

In this analysis, the locations of targets within the breast, as predicted by the SSHT FEM method, were compared to their actual locations. This was done as a function of the number of markers used. A PET image has a relatively low spatial resolution (approximately 5–7 mm), and reveals at best only the rough shape and size of the organ or tissue under consideration. It is therefore very difficult to define the same region of interest (target or landmark) precisely in both MR and PET images in order to perform the target registration error study. For this reason, we carried out target registration error studies using only high-resolution MRI data [25]. To accomplish this task, we first created an FEM mesh and defined an adequate number (15–25) of regions of interest (ROIs) over the entire breast spatial domain. Each of the selected ROIs contained a number of FEM nodes with known labels. Then, we defined a number of virtual fiducial skin markers in random locations and applied the SSHT FEM method to the FEM breast model to intentionally deform and subsequently to create a simulated target MR image. To assure realistic deformation, we used displacement vectors estimated in real scans for other subjects. We next localized the corresponding real fiducial skin markers in moving (MR) and intentionally deformed MR images, and estimated their displacement vectors. After that, we deformed the initial breast model again using the same mesh but with the observed displacement vectors loaded at real marker locations. We carried out this process for cases of nine, seven, five, four, and three fiducial markers. Because, in each case we deformed the same mesh, this procedure allowed us to keep track of the displacements of the labeled nodes belonging to the selected ROIs and to compare the predicted locations of the ROIs vs. calculated locations obtained using virtual FSMs. The observed differences provide estimates of the target registration errors. Examples of the ROIs distribution, in the error study of TRE vs. number of FSMs, are shown on the upper panels in Fig. 12. In addition to distribution of ROIs and FSMs, the graphs in the lower panels show polyhedra built by FSMs. They allow partitioning the ROIs into two classes: ROIs located inside and outside the volume bounded by the FSMs.

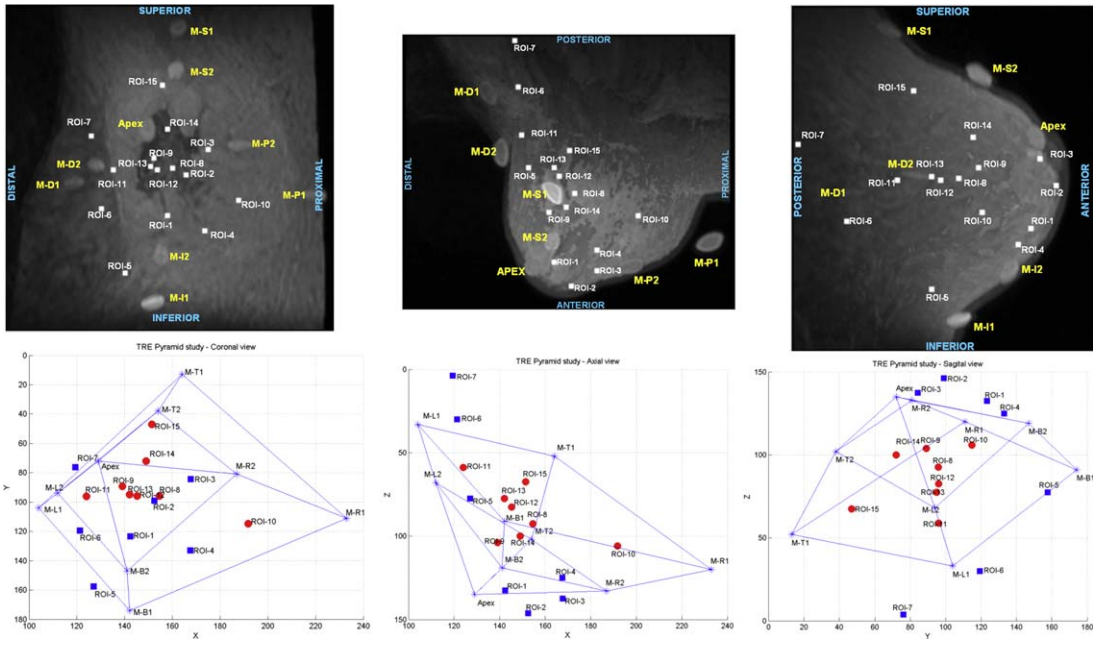

Fig. 12. Upper panel: location of selected ROIs and markers in MR breast image of Subject ♯4 used in studies of target registration error (TRE) vs. fiducial skin marker (FSM) location, in coronal, axial, and sagittal views, respectively. Lower panel: same ROIs in polyhedra defined by the markers. Red solid circles: ROIs inside the polyhedra. Blue solid squares: ROIs outside the polyhedra. For interpretation of the references to colour in this figure legend, the reader is referred to the web version of this article.

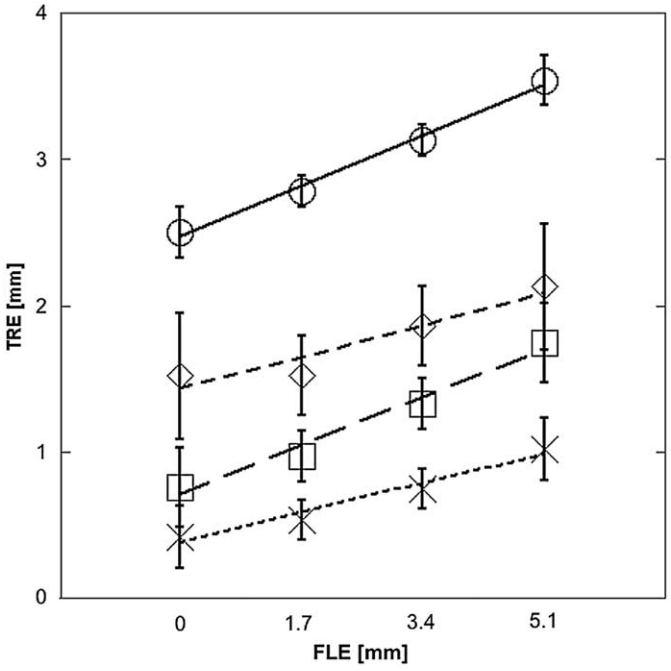

Fig. 13. Relationship between the average target registration error (TRE) and the number of markers used estimated for three randomly selected subjects. Circles: data for ROIs located outside the polyhedron defined by the fiducial skin markers, after our MR-to-PET registration (R^2=0.88, slope= −0.18 mm/marker with p=0.02). Diamonds: data for ROIs located outside the polyhedron after the optional MR-to-CT surface matching (R^2=0.67, slope= −0.13 mm/marker with p=0.09). Squares: data for ROIs located inside the polyhedron after our MR-to-PET registration (R^2=0.981, slope= −0.18 mm/marker with p=0.04). X symbols: data for ROIs located inside the polyhedron after the optional MR-to-CT surface matching (R^2=0.88, slope= −0.11 mm/marker with p=0.02). The error bars represent 90% confidence intervals.

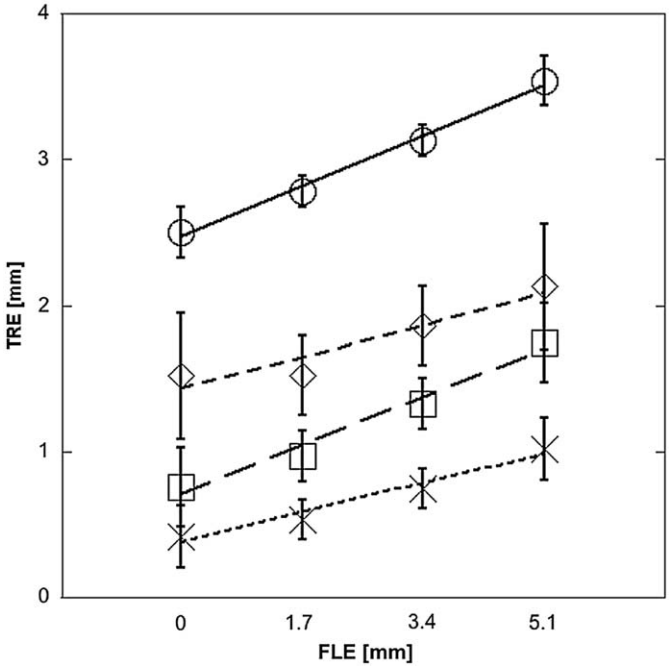

Fig. 14. Relationship between average target registration error (TRE) for three randomly selected subjects and fiducial localization error (FLE) estimated for nine FSMs per breast. Circles: data for ROIs located outside polyhedron defined by the fiducial skin markers, after our MR-to-PET registration (R^2=0.99, slope=0.35 mm/mm with p=0.003). Diamonds: data for ROIs located outside polyhedron after the optional MRI-to-CT surface matching (R^2=0.98, slope=0.22 mm/mm with p=0.051). Squares: data for ROIs located inside polyhedron after our MR-to-PET registration (R^2=0.90, slope=0.33 mm/mm with p=0.010). X symbols: data for ROIs located inside polyhedron after the optional MRI-to-CT surface matching (R^2=0.97, slope=0.20 mm/mm with p=0.016). The error bars represent 95% confidence intervals.

Fig. 13 shows the dependence of TRE on the number of markers used estimated for three randomly selected subjects. It is clear that: (i) the average target registration error for nine FSMs is below 3 mm in all the cases; (ii) TRE strongly depends on the number of markers used—it doubles for three FSMs vs. nine FSMs used per breast; and (iii) TRE depends strongly on FSM location, i.e. TRE is much higher for targets located outside the polyhedra formed by FSMs as compared to TRE for targets located inside the polyhedra. The latter finding can be explained by extrapolation used in the FEM simulations for the targets outside the polyhedra rather than interpolation used for the targets inside the polyhedra.

6.1.2. Target registration error vs. fiducial marker localization error

This analysis addresses the accuracy of estimating FSM locations (called fiducial localization error (FLE)) and its relationship with TRE. For each FSM, we introduced randomly oriented localization error vectors with amplitudes of 0, 1.7, 3.4, and 5.1 mm, respectively. The error increment of 1.7 mm was chosen to be one third of the MRI marker diameter. In the analysis, we used the data for the same subjects with the same ROIs as used in the study of TRE vs. number of FSMs.

The results obtained for nine FSMs per breast shown in Fig. 14 resemble plots of TRE vs. number of FSMs and can be summarized as follows: (i) the average TRE due to FLE is below 3 mm in all cases; (ii) TRE strongly depends on FSM location, i.e. TRE is much higher for targets located outside the polyhedron formed by FSMs; (iii) TRE increases with FLE; (iv) even in the case of FLE=5.1 mm, i.e. for error vector comparable with a physical size of MR fiducial marker, TRE is less than one PET voxel (4.25 mm).

6.1.3. Marker co-location error analysis

We also investigated the co-location error between the two sets of markers visible in MRI and PET by placing, removing, and placing again the selected markers, while leaving other markers in their original positions on patients in both PET and MRI scans. We then used the marker that was replaced as a target in our registration process. By applying this procedure, we determined that the mean FLE was below 2 mm.

6.1.4. Analysis of FEM solution convergence vs. number of nodes

The finite element method (FEM) software used in the study, ANSYS ver. 5.7.1, was limited to a maximum of 32,000 nodes. All our studies were done using this number of nodes. To investigate the convergence of the FEM model vs. number of nodes used, we performed a convergence analysis. TRE values were recorded while the number of nodes was increased gradually starting from 5000 until the maximum number of nodes was reached. The type of FEM mesh elements was kept the same while changing the number of nodes. Fig. 15 shows the relationship between average TRE estimated using 10 different ROIs vs. the number of nodes. We observe that change in the number of nodes from 5000 to 32,000 does not significantly affect TRE. Its value has changed merely from 1.63 to 1.49 mm, while the number of nodes has increased six-fold.

6.1.5. Estimation of breast tissue positioning error and related stress change in the breast

To evaluate the degree of similarity in positioning of the breast tissue between scans and the related stress change in the breast tissue, we performed an MRI scan, and asked the subject to leave the scanner and to return later for a second, identical MRI scan. The MRI fiducial skin markers were left attached to the breast. Using these data, we estimated that the mean displacement of fiducial skin markers due to repositioning in the scanner was 11.5 ± 3.0 mm, resulting in an estimated (24 ± 4)% relative breast strain change. Consequently, using strain–stress relationship provided by Wellman [60] and Azar [61], the estimated corresponding relative stress change in the breast is (37 ± 2)%.

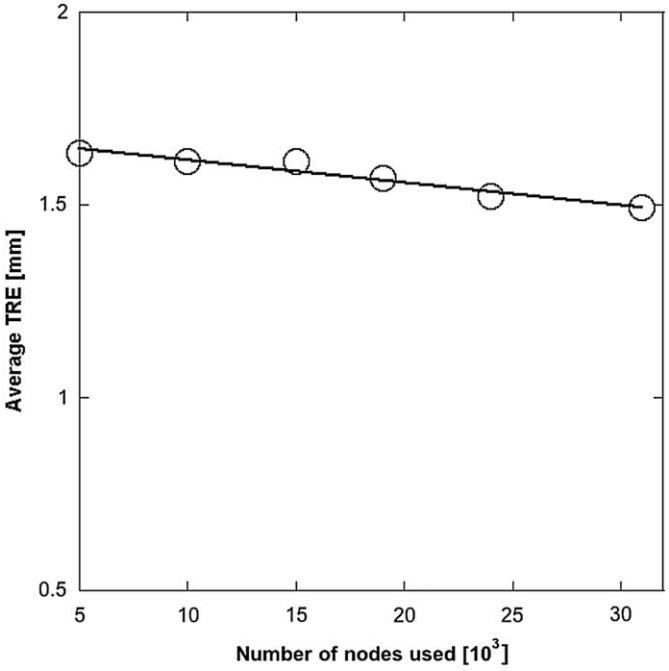

Fig. 15. Example of the relationship between average target registration error (TRE) and number of nodes used in our FEM registration method estimated for Subject ♯1 (R^2=0.97, slope= −0.0058 mm per number of nodes with p=0.0016).

6.2. Intensity-based similarity metrics

Two intensity-based similarity metrics, mutual information (MI) and normalized mutual information (NMI), were used to evaluate the similarity between MR and PET breast images before and after application of our FEM-based registration method (Table 6). Mutual information is a commonly used similarity metric in image registration applications. It reaches its maximum when two images are geometrically aligned but is sensitive to the amount of overlap between the images [69–71]. Studholme et al. introduced normalized mutual information (NMI) that accounts for the degree of overlap between the two images and hence it is more suitable for MR-to-PET registration quality evaluation [71].

The results collected in Table 6 demonstrate that our nonrigid iterative multimodality breast-image registration method yielded improvement in MI and NMI metrics for all 15 subjects, as compared to rigid registration. However, the second iteration of our method yielded statistically insignificant similarity values degradation, as compared to the first iteration. It can be explained by an increase in the uncertainty in MI and NMI estimation after the second iteration in our registration method due to application of image warping for the second time. We recall that image warping requires image intensity interpolation.

6.3. Qualitative surface similarity estimates

To evaluate our results qualitatively, we implemented three different similarity measurement plots:

(i) isoprojected surface similarity (ISS),
(ii) normalized polar surface similarity (NPSS),
(iii) z-axis surface similarity (ZSS).

The ISS plot is a surface projection image that represents distances between the corresponding points on the moving (MR) and the target (PET) image surfaces with the same z-axis coordinate as an intensity value. In Fig. 16, as an example, we present the ISS plots for the first three subjects. The results for other subjects are very similar. Here the amount of misregistration (i.e. the distance between the corresponding

Table 6
Calculated image similarity values.

Subject	After rigid registration		After SSHT FEM first iteration		After SSHT FEM second iteration	
	MI	NMI	MI	NMI	MI	NMI
1	1.22	1.10	2.63	1.22	2.85	1.24
2	1.48	1.12	2.09	1.17	2.26	1.19
3	1.40	1.12	1.56	1.13	1.39	1.11
4	1.56	1.15	3.23	1.31	3.22	1.31
5	1.20	1.10	2.57	1.22	2.86	1.26
6	1.34	1.11	2.09	1.17	1.87	1.15
7	1.32	1.11	1.55	1.13	1.76	1.15
8	1.48	1.13	2.09	1.17	1.83	1.15
9	0.58	1.05	4.16	1.51	4.18	1.52
10	2.36	1.22	3.11	1.28	N/A	N/A
11	1.34	1.12	2.63	1.23	2.20	1.18
12	1.83	1.17	4.28	1.42	3.86	1.37
13	1.33	1.11	3.35	1.29	3.29	1.28
14	0.38	1.03	4.41	1.44	4.45	1.44
15	1.76	1.15	3.65	1.32	3.54	1.30
Mean ± S.D.	1.372 ± 0.468	1.119 ± 0.045	2.893 ± 0.946	1.267 ± 0.116	2.637 ± 1.186	1.177 ± 0.345
Best value:	Maximum value for two specific images	2.0	Maximum value for two specific images	2.0	Maximum value for two specific images	2.0

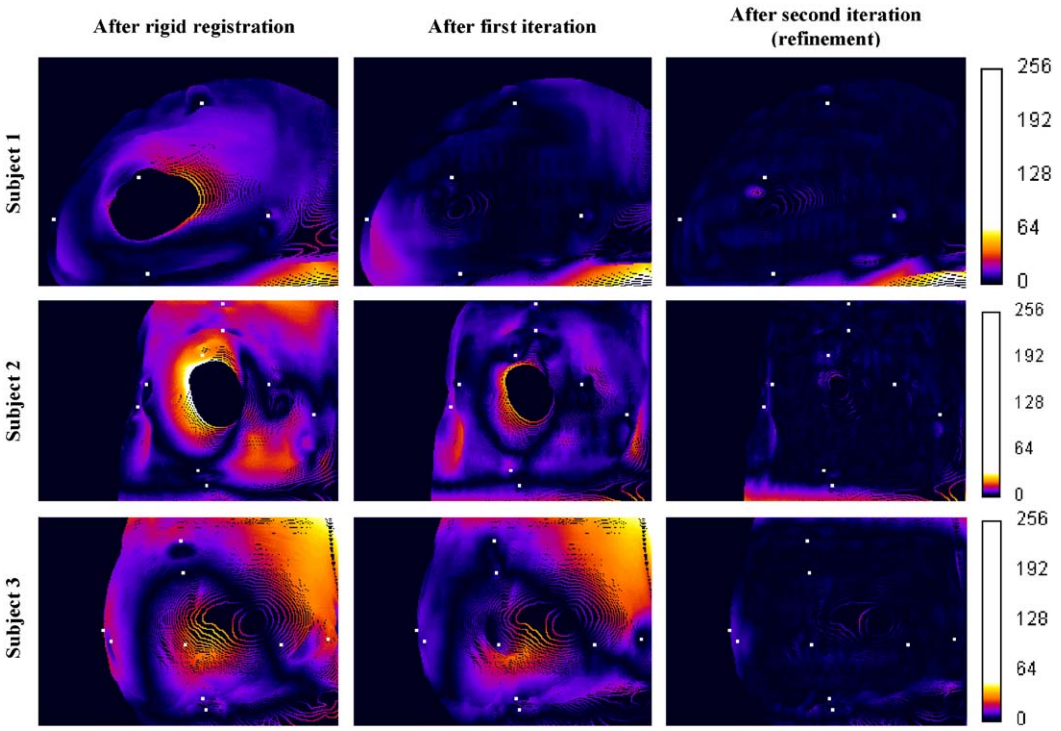

Fig. 16. Isoprojected surface similarity (ISS) plots for the right breast obtained for three subjects participating in this study displayed using RGB values in "fire" LUT. White dots represent projections of the fiducial skin markers on a common plane.

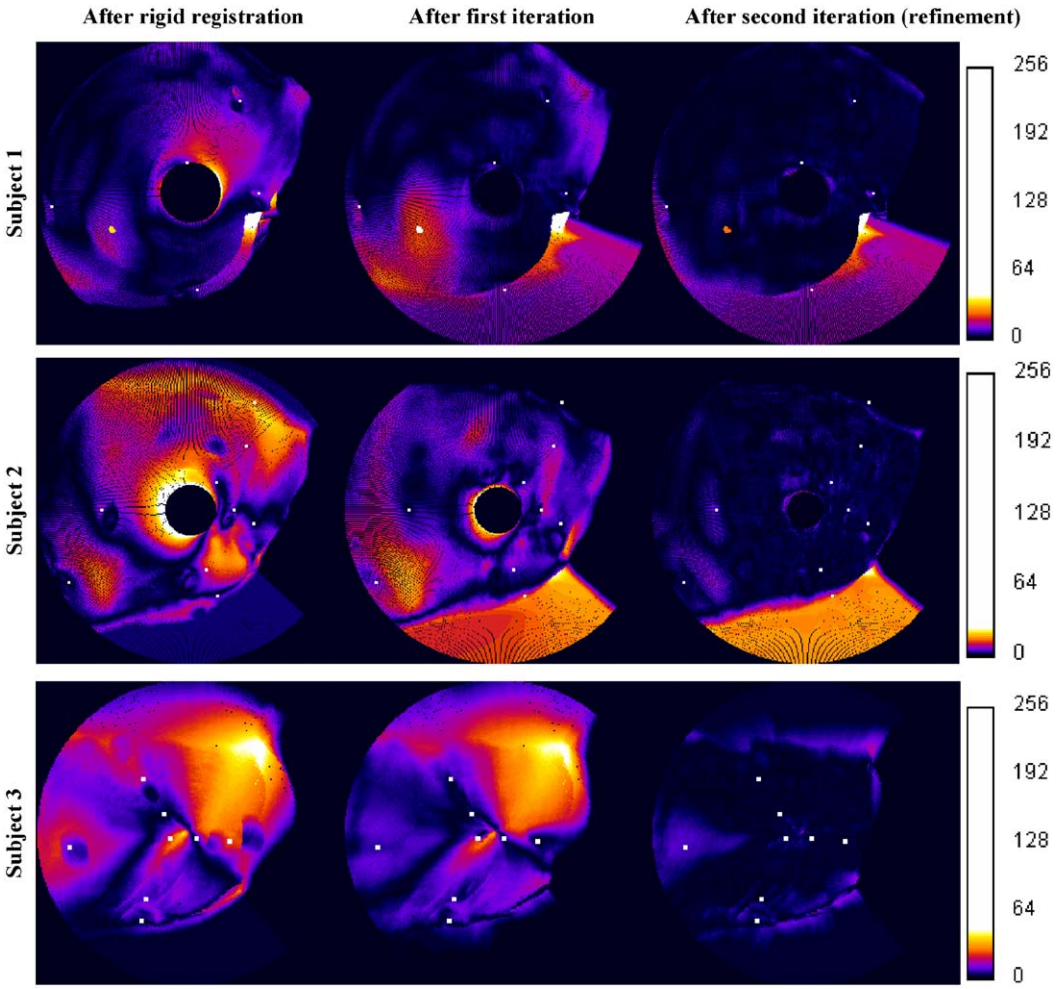

Fig. 17. Normalized polar surface similarity (NPSS) plots for the right breast obtained for three subjects participating in this study. White dots represent projections of the fiducial skin markers on a common plane.

surface points on the moving, MR, and the target, PET, images), is related to RGB values in the "fire" LUT and two perfectly registered images would produce a uniformly black ISS image. We performed ISS analyses for all subjects and observed improvement in the surface registration for all of them.

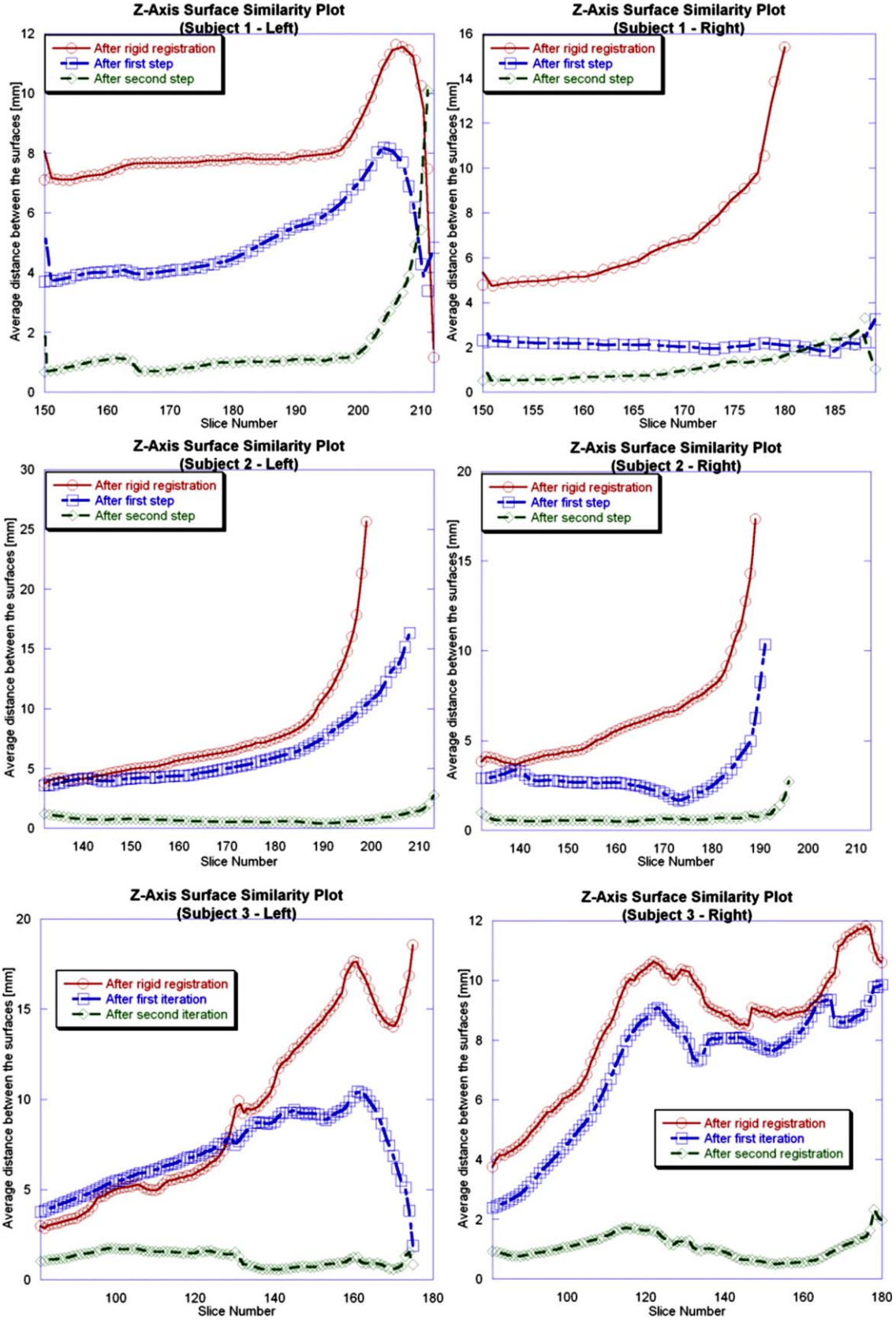

Fig. 18. *z*-Axis surface similarity plots obtained for three subjects participating in this study.

The NPSS plot is similar to the ISS plot except that it is a polar isoprojection of the distances between the corresponding points on the moving (MR) and the target (PET) image surfaces. Its center corresponds to the apex section of the imaged breast. It is analogous to a polar plot (bull's-eye plot) widely used in the myocardial perfusion imaging [72]. NPSS allows comparison of registration quality obtained for different subjects. In Fig. 17, as an example, we show the NPSS plots for the same three subjects as shown in Fig. 16. We performed NPSS analyses for all subjects and observed comparable improvement in the surface registration for all of them.

ZSS is a graph, which represents the average distance between the corresponding points on the moving and the target image surfaces with the same z-axis coordinate vs. z. The ZSS plots were obtained by comparing the moving (MR) and the target (PET) image surfaces slice by slice in coronal views. In Fig. 18, as an example, we show the ZSS plots for the same three subjects as shown in Fig. 16. We performed ZSS analyses for all subjects and observed improvement in the surface registration for all of them.

7. Conclusions

We have developed and tested a new simple computerized finite element method (FEM) approach for 3D nonrigid registration of PET and MR breast images. It requires five to nine fiducial skin markers visible in MRI and PET placed on previously marked locations on the breast surface during both scans, but contrary to other published FEM approaches it does not require difficult-to-obtain, patient-specific mechanical properties of the breast tissue. In addition, during PET scan it is necessary to position patient prone, using a plastic replica of the MRI breast coil, similarly to the MR scan. We have verified that small errors in patient positioning do not create problems for the registration process. We demonstrated that under such conditions, the observed displacement vectors defined by corresponding pairs of fiducial skin markers between MR and PET images, distributed piecewise linearly over the breast volume, produce a deformed FEM mesh that reasonably approximates nonrigid deformation of the breast tissue between the MRI and PET scans. We emphasize that this method does not require a biomechanical breast tissue model and results in the target registration error (TRE) that is below 4 mm, i.e. much below the spatial resolution of PET scanner that is in the range 6–7 mm. If coregistered CT data are available in addition to PET (e.g. from a PET/CT scanner) then an optional MR-to-CT surface matching can be performed further lowering TRE to below 3 mm. The registration errors of our approach are smaller than those obtained by application of the state-of-the art registration methods reported by Somers et al. [29] who used the same model of PET/CT scanner (Discovery ST) as we did for soft-tissue sarcoma imaging. They reported TRE of 9.0 and 14.1 mm for direct rigid registration of MR-to-PET images using external fiducial markers and the voxel-intensity method, respectively, and TRE of 8.5 mm for hybrid (indirect) registration that employed the MR-to-CT derived transformation to the MR-to-PET registration task.

Because of budgetary constraints, we tested our method on MR and PET/CT breast images acquired for 15 subjects only. We plan to increase the number of subjects in the future, in order to increase the statistical power of the study and to confirm the validity of our method.

We have observed perfect registration of all fiducial skin markers visible in MRI to corresponding fiducial skin markers visible in PET and improved registration of the enhanced metabolic activity regions revealed by PET with the well-defined glandular tissue regions demonstrated by high-resolution MRI. Contrary to other methods such as utilizing voxel intensity-based similarity measures or surface matching, our method works for matching MR with pure molecular images (e.g. PET only), even without coregistered CT images from a PET/CT scanner. Our method does not require a good initialization and would not be trapped by local minima during a registration process. All processing including FSMs detection and matching, and mesh generation can be fully automated. All the computations can be finished in about 15 min on a commonly available workstation. Based on the results obtained for 15 subjects studied to date, we conclude that this is a very fast and well-performing method for MR-to-PET breast-image nonrigid registration. Consequently, it is a promising approach in clinical practice. This method can be easily applied to nonrigid registration of MRI or CT of any type of soft-tissue images to their molecular counterparts such as obtained using PET or SPECT.

It is known that the combination of functional and molecular data from multiple sources (e.g. dynamic MR and molecular imaging), along with complementary anatomic information provided by MRI and CT, increases the diagnostic efficacy for breast cancer detection, staging, and assessment of the response to therapy. Therefore, the availability of a robust and fast registration method for breast PET and breast MRI, would allow clinical implementation of multimodality imaging of the breast and other soft tissues.

Acknowledgments

This work was partially supported by grants from the Carol M. Baldwin Breast Cancer Research Foundation of Central New York, and from the Department of Radiology, SUNY Upstate Medical University. M.Z. Unlu was supported by a grant from Turkish Ministry of National Education and by Syracuse University.

We would like to express our gratitude to Ms. Gwen Tillapaugh-Fay for performing MRI scans, to Ms. Wendy McGraw for performing PET scans, to Dr. Nikolaus Szeverenyi for his help in creating MRI fiducial skin markers, and to Dr. Stefan Siegel from Siemens Preclinical Solutions (formerly CTI Molecular Imaging) for supplying PET fiducial skin markers.

Conflict of interest statement

None declared

References

[1] C.C. Boring, T.S. Squires, T. Tong, S. Montgomery, Cancer statistics, CA: A Cancer Journal for Clinicians 44 (1) (1994) 7–26.
[2] What are the key statistics for breast cancer? American Cancer Society, http://www.cancer.org, (2007).
[3] A. Mendez, F. Cabanillaz, Evaluation of breast imaging reporting and data system category 3 mammograms and the use of stereotactic vacuum-assisted breast biopsy in a nonacademic community practice, Cancer 100 (2004) 710–714.
[4] L. Delle Chiaie, R. Terinde, Three-dimensional ultrasound-validated large-core needle biopsy: is it a reliable method for the histological assessment of breast lesions?, Ultrasound in Obstetrics and Gynecology 23 (4) (2004) 393–397.
[5] A.R. Carmichel, A. Berresford, Imprint cytology of needle core-biopsy specimens of breast lesion: is it best of both worlds?, Breast 13 (2004) 232–234.
[6] J.H. Burkhardt, J.H. Sunshine, Core-needle and surgical breast biopsy: comparison of three methods of assessing cost, Radiology 212 (1999) 181–188.
[7] M. Bloomston, P. D'Angelo, D. Galliano, J.B. Jr, R. Dean, A.S. Rosemurgy, One hundred consecutive advanced breast biopsy instrumentation procedures: complications, costs, and outcome, Annals of Surgical Oncology 6 (2) (1999) 195–199.
[8] L.E. Philpotts, R.J. Hooley, C.H. Lee, Comparison of automated versus vacuum-assisted biopsy methods for sonographically guided core biopsy of the breast, American Journal of Roentgenology 180 (2) (2002) 347–351.

[9] K. Scheidhauer, C. Walter, M.D. Seemann, FDG PET and other imaging modalities in the primary diagnosis of suspicious breast lesions, European Journal of Nuclear Medicine and Molecular Imaging 31 (Suppl. 1) (2004) S70–S79.
[10] E. Bombardieri, F. Crippa, PET imaging in breast cancer, Quarterly Journal of Nuclear Medicine 45 (3) (2001) 245–256.
[11] G.W. Gorres, H.C. Steinert, G.K.V. Schulthess, PET and functional anatomic fusion imaging in lung and breast cancers, The Cancer Journal 10 (4) (2004) 251–261.
[12] S. Beaulieu, P. Kinahan, J. Tseng, L.K. Dunnwald, E.K. Schubert, P. Pham, B. Lewellen, D.A. Mankoff, SUV varies with time after injection in 18F-FDG PET of breast cancer: characterization and method to adjust for time differences, Journal of Nuclear Medicine 44 (7) (2003) 1044–1050.
[13] W.B. Eubank, D. Mankoff, M. Bhattacharya, J. Gralow, H. Linden, G. Ellis, S. Lindsley, M. Austin-Seymour, R. Livingston, Impact of FDG PET on defining the extent of disease and on the treatment of patients with recurrent or metastatic breast cancer, American Journal of Roentgenology 183 (2) (2004) 479–486.
[14] K. Kinkel, N.M. Hylton, Challenges to interpretation of breast MRI, Journal of Magnetic Resonance Imaging 13 (2001) 830–836.
[15] F. Baum, U. Fischer, R. Vosshenrich, E. Grabbe, Classification of hypervascularized lesions in CE MR imaging of the breast, European Radiology 12 (5) (2002) 1087–1092.
[16] L. Moy, F. Ponzo, M.E. Noz, G.Q.M. Jr, A.D. Murphy-Walcott, A.E. Deans, M.T. Kitazono, L. Travascio, E.L. Kramer, Improving specificity of breast MRI using prone PET and fused MRI and PET 3D volume data sets, Journal of Nuclear Medicine 48 (4) (2007) 528–537.
[17] A. Rieber, H. Schirrmeister, A. Gabelmann, K. Nuessle, S. Reske, R. Kreienberg, H.J. Brambs, T. Kuehn, Pre-operative staging of invasive breast cancer with MR mammography and/or PET: boon or bunk?, The British Journal of Radiology 75 (2002) 789–798.
[18] C. Walter, K. Scheidhauer, A. Scharl, U.-J. Goering, P. Theissen, H. Kugel, T. Krahe, U. Pietrzyk, Clinical and diagnostic value of preoperative MR mammography and FDG-PET in suspicious breast lesions, European Radiology 13 (2003) 1651–1656.
[19] L. Moy, M.E. Noz, G.Q.M. Jr, F. Ponzo, A.E. Deans, A.D. Murphy-Walcott, E.L. Kramer, Prone mammoPET acquisition improves the ability to fuse MRI and PET breast scans, Clinical Nuclear Medicine 32 (3) (2007) 194–198.
[20] C. Catana, Y. Wu, M.S. Judenhofer, J. Qi, B.J. Pichler, S.R. Cherry, Simultaneous acquisition of multislice PET and MR images: Initial results with a MR-compatible PET scanner, Journal of Nuclear Medicine 47 (2006) 1968–1976.
[21] B.J. Pichler, M.S. Judenhofer, C. Catana, J.H. Walton, M. Kneilling, R.E. Nutt, S.B. Siegel, C.D. Claussen, S.R. Cherry, Performance test of an LSO-APD detector in a 7-T MRI scanner for simultaneous PET/MRI, Journal of Nuclear Medicine 47 (4) (2006) 639–647.
[22] J.B.A. Maintz, E.H.W. Meijering, M.A. Viergever, General multimodal elastic registration based on mutual information, in: Proceedings of the SPIE Medical Imaging: Image Processing, 1998, Bellingham, WA, 3338 (1998) 144–154.
[23] J.B.A. Maintz, M.A. Viergever, A survey of medical image registration, Medical Image Analysis 2 (1) (1998) 1–36.
[24] I. Bankman, Handbook of Medical Imaging: Processing and Analysis (Biomedical Engineering) (Hardcover), vol. Chapter 29: Wood, 2000.
[25] J.V. Hajnal, D.L.G. Hill, D.J. Hawkes, Medical Image Registration (Biomedical Engineering), first ed., CRC, London, UK, 2001.
[26] T.S. Yoo, Insight into Images: Principles and Practice for Segmentation, Registration, and Image Analysis (Hardcover), first ed., AK Peters, 2004.
[27] L. Hallpike, D.J. Hawkes, Medical image registration: an overview, Imaging 14 (2002) 455–463.
[28] H. Chui, A. Rangarajan, A new point matching algorithm for non-rigid registration, Computer Vision and Image Understanding 89 (2–3) (2003) 114–141.
[29] E.J. Somer, N.A. Benatar, M.J. O'Doherty, M.A. Smith, P.K. Marsden, Use of the CT component of PET–CT to improve PET–MR registration: demonstration in soft-tissue sarcoma, Physics in Medicine and Biology 52 (2007) 6991–7006.
[30] C.S. Zuo, A. Jiang, B.L. Buff, T.G. Mahon, T.Z. Wong, Automatic motion correction for breast MR imaging, Radiology 198 (3) (1996) 903–906.
[31] R.P. Woods, J.C. Mazziotta, S.R. Cherry, MRI–PET registration with automated algorithm, Journal of Computer Assisted Tomography 17 (4) (1993) 536–546.
[32] R. Kumar, J.C. Asmuth, K. Hanna, J.R. Bergen, C. Hulka, D.B. Kopans, R. Weisskoff, R.H. Moore, Application of 3D registration for detecting lesions in magnetic resonance scans, in: Proceedings of the SPIE Medical Imaging: Image Processing, 1996, USA, 2710 (1996) 646–656.
[33] D. Rueckert, L.I. Sonoda, C. Hayes, D.L. Hill, M.O. Leach, D.J. Hawkes, Nonrigid registration using free-form deformations: application to breast MR images, IEEE Transactions on Medical Imaging 18 (8) (1999) 712–721.
[34] T. Rohlfing, C.R. Maurer Jr., D.A. Bluemke, M.A. Jacobs, Volume-preserving nonrigid registration of MR breast images using free-form deformation with an incompressibility constraint, IEEE Transactions on Medical Imaging 22 (6) (2003) 730–741.
[35] C. Tanner, J.A. Schnabel, D.L. Hill, D.J. Hawkes, A. Degenhard, M.O. Leach, D.R. Hose, M.A. Hall-Craggs, S.I. Usiskin, Quantitative evaluation of free-form deformation registration for dynamic contrast-enhanced MR mammography, Medical Physics 34 (4) (2007) 1221–1233.
[36] W.R. Crum, C. Tanner, D.J. Hawkes, Anisotropic multi-scale fluid registration: evaluation in magnetic resonance breast imaging, Physics in Medicine and Biology 50 (21) (2005) 5153–5174.
[37] M.S. Froh, D.C. Barber, K.K. Brock, D.B. Plewes, A.L. Martel, Piecewise-quadrilateral registration by optical flow—applications in contrast-enhanced MR imaging of the breast, Medical Image Computing and Computer-assisted Intervention—MICCAI 2006, Lecture Notes in Computer Science, vol. 9, Springer-Verlag, Berlin/Heidelberg, 2006, pp. 686–693.
[38] A. Krol, I.L. Coman, J.A. Mandel, M. Luo, D.H. Feiglin, E.D. Lipson, J. Beaumont, Inter-modality nonrigid breast image registration using finite-element method, in: Proceedings of the IEEE Nuclear Science Symposium and Medical Imaging Conference, October 19–25, 2003, Portland, OR, 3 (2003) 1958–1961.
[39] I.L. Coman, A. Krol, D.H. Feiglin, E.D. Lipson, J.A. Mandel, K.G. Baum, M.Z. Unlu, W. Lee, Intermodality nonrigid breast-image registration, in: Proceedings of the IEEE International Symposium on Biomedical Imaging, ISBI 2004 From Nano to Macro, 15–18 April 2004, 2 (2004) 1440–1442.
[40] I.L. Coman, A. Krol, J.A. Mandel, K.G. Baum, M. Luo, E.D. Lipson, D.H. Feiglin, Finite-element method for intermodality nonrigid breast registration using external skin markers, in: Proceedings of the SPIE Medical Imaging: Image Processing, San Diego, CA, 5370 (2004) 1152–1155.
[41] A. Krol, M.Z. Unlu, K.G. Baum, J.A. Mandel, W. Lee, I.L. Coman, E.D. Lipson, D.H. Feiglin, MRI/PET nonrigid breast-image registration using fiducial skin markers, Physica Medica 21 (Suppl. 1) (2006) 39–43.
[42] A. Krol, M.Z. Unlu, A. Magri, E. Lipson, I.L. Coman, J.A. Mandel, K.G. Baum, D.H. Feiglin, Iterative finite element deformable model for nonrigid coregistration of multimodal breast images, in: Proceedings of the Biomedical Imaging: Nano to Macro, 2006., third ed., IEEE International Symposium on, USA, 2006, pp. 852–855.
[43] M.E. Noz, G.Q.M. Jr., L. Moy, F. Ponzo, E.L. Kramer, Can the specificity of MRI breast imaging be improved by fusing 3D MRI volume data sets with FDG PET? in: Proceedings of the IEEE International Symposium on Biomedical Imaging: Nano to Macro, 15–18 April 2004, 2 (2004) 1388–1391.
[44] E.L. Kramer, M.E. Noz, CT/SPECT fusion for analysis of radiolabeled antibodies: applications in gastrointestinal and lung carcinoma, International Journal of Radiation Applications and Instrumentation, Part B Nuclear Medicine and Biology 18 (1) (1991) 27–42.
[45] A.D. Castellano-Smith, T. Hartkens, J.A. Schnabel, D.R. Hose, H. Liu, W.A. Hall, C.L. Truwit, D.J. Hawkes, D.L.G. Hill, Constructing patient specific models for correcting intraoperative brain deformation, Medical Image Computing and Computer-assisted Intervention—MICCAI 2001, Lecture Notes in Computer Science, vol. 2208, Springer-Verlag, Berlin/Heidelberg, 2001, pp. 1091–1098.
[46] M. Ferrant, A. Nabavi, B. Macq, F.A. Jolesz, R. Kikinis, S.K. Warfield, Registration of 3-D intraoperative MR images of the brain using a finite-element biomechanical model, IEEE Transactions on Medical Imaging 20 (12) (2001) 1384–1397.
[47] M. Sermesant, H. Delingette, N. Ayache, An electromechanical model of the heart for image analysis and simulation, IEEE Transactions on Medical Imaging 25 (5) (2006) 612–625.
[48] V. Zagrodsky, V. Walimbe, C.R. Castro-Pareja, J.X. Qin, J.-M. Song, R. Shekhar, Registration-assisted segmentation of real-time 3-D echocardiographic data using deformable models, IEEE Transactions on Medical Imaging 24 (9) (2005) 1089–1099.
[49] F.S. Azar, D.N. Metaxas, M.D. Schnall, A deformable finite element model of the breast for predicting mechanical deformations under external perturbations, Academic Radiology 8 (10) (2001) 965–975.
[50] A. Sitek, J.G. Klein, T.G. Gullberg, H.R. Huesman, Deformable model of the heart with fiber structure, IEEE Transactions on Nuclear Science 49 (3) (2002) 789–793.
[51] F.S. Azar, D.N. Metaxas, M.D. Schnall, Methods for modeling and predicting mechanical deformations of the breast under external perturbations, Medical Image Analysis 6 (1) (2002) 1–27.
[52] F.S. Azar, D.N. Metaxas, M.D. Schnall, A finite model of the breast for predicting mechanical deformations during biopsy procedure, in: Proceedings of the IEEE Workshop Mathematical Methods in Biomedical Image Analysis, June, 2000 (2000) 38–45.
[53] N.V. Ruiter, R. Stotzka, T.-O. Müller, H. Gemmeke, J.R. Reichenbach, W.A. Kaiser, Model-based registration of X-ray mammograms and MR images of the female breast, IEEE Transactions on Nuclear Science 53 (1) (2006) 204–211.
[54] F.J.P. Richard, P.R. Bakie, A.D.A. Maidment, Mammogram registration: a phantom-based evaluation of compressed breast thickness variation effects, IEEE Transactions on Medical Imaging 25 (2) (2006) 188–197.
[55] A. Samani, J. Bishop, M.J. Yaffe, D.B. Plewes, Biomechanical 3-D finite element modeling of the human breast using MRI data, IEEE Transactions on Medical Imaging 20 (4) (2001) 271–279.
[56] J.A. Schnabel, C. Tanner, A.D. Castellano-Smith, A. Degenhard, M.O. Leach, D.R. Hose, D.L.G. Hill, D.J. Hawkes, Validation of nonrigid image registration using finite-element methods: application to breast MR images, IEEE Transactions of Medical Imaging 22 (2) (2003) 238–247.
[57] L. Roose, W. Mollemans, D. Loeckx, F. Maes, P. Suetens, Biomechanically based elastic breast registration using mass tensor simulation, Medical Image Computing and Computer-assisted Intervention—MICCAI 2006, Lecture Notes in Computer Science, vol. 4191, Springer, Berlin/Heidelberg, 2006, pp. 718–725.
[58] N.V. Ruiter, Registration of X-ray Mammograms and MR-volumes of the Female Breast Based on Simulated Mammographic Deformation, Ph.D. Thesis, Universitat Mannheim, Mannheim, 2003.

[59] V. Rajagopal, J. Chung, P.M.F. Nielsen, M.P. Nash, Finite element modeling of breast biomechanics: directly calculating the reference state, in: Proceedings of the Engineering in Medicine and Biology Society, 2006. EMBS '06. 28th Annual International Conference of the IEEE (2006) 420–423.
[60] P.S. Wellman, Tactile Imaging, Thesis, Harvard University, Cambridge MA, 1999.
[61] F.S. Azar, A Deformable Finite Element Model of the Breast for Predicting Mechanical Deformations under External Perturbations, Ph.D. Thesis, Department of Bioengineering, University of Pennsylvania, Philadelphia, PA, 2001.
[62] P. Jazzard, Physical basis of spatial distortion in MRI, in: I.N. Bankman (Ed.), Handbook of Medical Imaging, vol. 1, Academic Press, 2000.
[63] M. Dahlbom, S.C. Huang, Physical and biological bases of spatial distortion in PET images, in: I.N. Bankman (Ed.), Handbook of Medical Imaging, Academic Press, 2000.
[64] M.Y. Wang, C.R. Maurer Jr., J.M. Fitzpatrick, R.J. Maciunas, An automatic technique for finding and localizing externally attached markers in CT and MR volume images of the head, IEEE Transactions on Biomedical Engineering 43 (6) (1996) 627–637.
[65] D.J. Walvoord, K. Baum, M. Helguera, A. Krol, R.L. Easton, Localization of fiducial skin markers in MR images using correlation pattern recognition for PET/MRI nonrigid breast image registration, in: Proceedings of the Applied Imagery Pattern Recognition (AIPR) Annual Workshop (2009).
[66] T.F. Chan, L.A. Vese, Active contours without edges, IEEE Transactions on Image Processing 10 (2) (2001) 266–277.
[67] O.C. Zienkiewicz, R.L. Taylor, The Finite Element Method, third ed., McGraw Hill Book Co., New York, 1977.
[68] E.H.W. Meijering, W.J. Niessen, J.P.W. Pluim, M.A. Viergever, Quantitative comparison of Sinc-approximating kernels for medical image interpolation, in: C. Taylor, A. Colchester (Eds.), Medical Image Computing and Computer-assisted Intervention—MICCAI'99, Lecture Notes in Computer Science, vol. 1679, Springer-Verlag, Berlin/Heidelberg, 1999, pp. 210–217.
[69] J.P. Pluim, J.B. Maintz, M.A. Viergever, Mutual-information-based registration of medical images: a survey, IEEE Transactions of Medical Imaging 22 (8) (2003) 986–1004.
[70] C. Studholme, Measures of 3D Medical Image Alignment, Ph.D. Thesis, University of London, London, 1997.
[71] C. Studholme, D.L.G. Hill, D.J. Hawkes, An overlap invariant entropy measure of 3D medical image alignment, Pattern Recognition 32 (1) (1999) 71–86.
[72] M. Minoves, A. Garcia, J. Magrina, J. Pavia, R. Herranz, J. Setoain, Evaluation of myocardial perfusion defects by means of "bull's eye" images, Clinical Cardiology 16 (1) (1993) 16–22.

Mehmet Z. Unlu received the B.Sc. degree in electronic's engineering from Ankara University, Ankara, Turkey, in 1994, the M.Sc. degree in electrical engineering from the University of Pittsburgh, Pittsburgh, PA, in 2001 and the Ph.D. degree in electrical engineering from Syracuse University, Syracuse, NY in May 2006. From 2001 to 2006, he was a research and teaching assistant at Syracuse University. Since November 2006, he has been an Assistant Professor with the Department of Electrical and Electronics Engineering at Izmir Institute of Technology, Izmir, Turkey. His main area of interest is medical image and signal processing. In 1999, he was awarded a multi-year scholarship for his Ph.D. education in the US from the Turkish Ministry of National Education, and in 2006 he received a university doctoral prize for his Ph.D. dissertation and study at Syracuse University.